Supplemental Information

Identification of advanced spin-driven thermoelectric materials via interpretable machine learning

Yuma Iwasaki [1,2]*, Ryohto Sawada [1], Valentin Stanev [3,4,5], Masahiko Ishida [1], Akihiro Kirihara [1], Yasutomo Omori [1], Hiroko Someya [1], Ichiro Takeuchi [3], Eiji Saitoh [6,7,8], Shinichi Yorozu [9]

[1]Central Research Laboratories, NEC Corporation, Tsukuba 305-8501, Japan

[2]PREST, JST, Saitama 322-0012, Japan

[3]Department of Materials Science and Engineering, University of Maryland, College park, MD 20742, USA

[4]*Center for Nanophysics and Advanced Materials, University of Maryland, College Park, MD 20742, USA*

[5]Joint Quantum Institute, University of Maryland, College Park, MD, 20742, USA

[6]Institute for Materials Research, Tohoku University, Sendai 908-8577, Japan

[7]WPI Advanced Institute for Materials Research, Tohoku University, Sendai 908-8577, Japan

[8]Advanced Science Research Center, Japan Atomic Energy Agency, Tokai, 319-1195, Japan

[9]RIKEN Center for Emergent Matter Science, Wako 351-0198, Japan

Email: y-iwasaki@ih.jp.nec.com

Supplementary Methods

The thermopower S_{STE} of the magnetic materials (FePt, CoPt, and NiPt binary alloys) were obtained by combinatorial technologies that enable us to obtain a lot of experimental material data in a short time [1,2]. The thin films of the magnetic materials were fabricated on the Silicon (Si), Aluminum Nitride (AlN), and Gadolinium Gallium Garnet (GGG) single crystal substrates by a combinatorial sputtering deposition technique [2]. Supplementary Figure 1(a) shows an image of the combinatorial sputtering system, in which the composition spread thin film is formed along the x direction due to the two tilted guns (cathodes). The deposition processes were performed in 0.3 Pa Ar-atmosphere at room temperature. The post-annealing process was carried out in vacuum ($< 2.5 \times 10^{-6}$ Pa) at 600 °C for 1 hour. The combinatorial X-ray fluorescence (XRF) measurement [2] and combinatorial X-ray diffraction (XRD) measurement [2] were performed to obtain composition and crystal structure information on the different points in the composition spread thin film. To measure the thermopower S_{STE}, this sample was cut into a lot of small tips, as shown in Supplementary Figure 1(b). The L_x, L_y and L_z^{film} are 2 mm, 8 mm, and 150 nm, respectively. The substrate thickness $L_z^{sub.}$ of Si, AlN, and GGG are 381 μm, 450 μm, and 500 μm, respectively. A temperature difference ΔT was applied between the top and bottom of the tips by sandwiching the tips between copper heat baths at 300 K and 300+ΔT K. Magnetic field H was applied along the x direction. Under these conditions, the spin-driven thermoelectric voltage V_{STE} can be detected along the y direction. The distances between the voltage-detection terminals were set to 6 mm. Supplementary Figure 1 (c) shows typical the V_{STE} behaviors of the $Ni_{88.3}Pt_{11.7}$/GGG sample as a function of H for different ΔT. Note that the sign of V_{STE} changes when the sign of H is inverted – a clear indication that the thermoelectric voltage arises from the anomalous Nernst effect (ANE) [3]. The thermopower S_{STE} is calculated as $S_{STE} = (V_{STE}/\Delta T)\left(L_z^{sub.}/L_y\right)$ [4].

The experimental condition term $\mathbf{C} \equiv \{AlN, Si, GGG\}$, the substrates used in the material fabrication process, is converted into binary $\{0,1\}$. For instance, when we use the Si substrate for the material fabrication process, the parameters are set to $\{C_{AlN}, C_{Si}, C_{GGG}\} = \{0, 1, 0\}$.

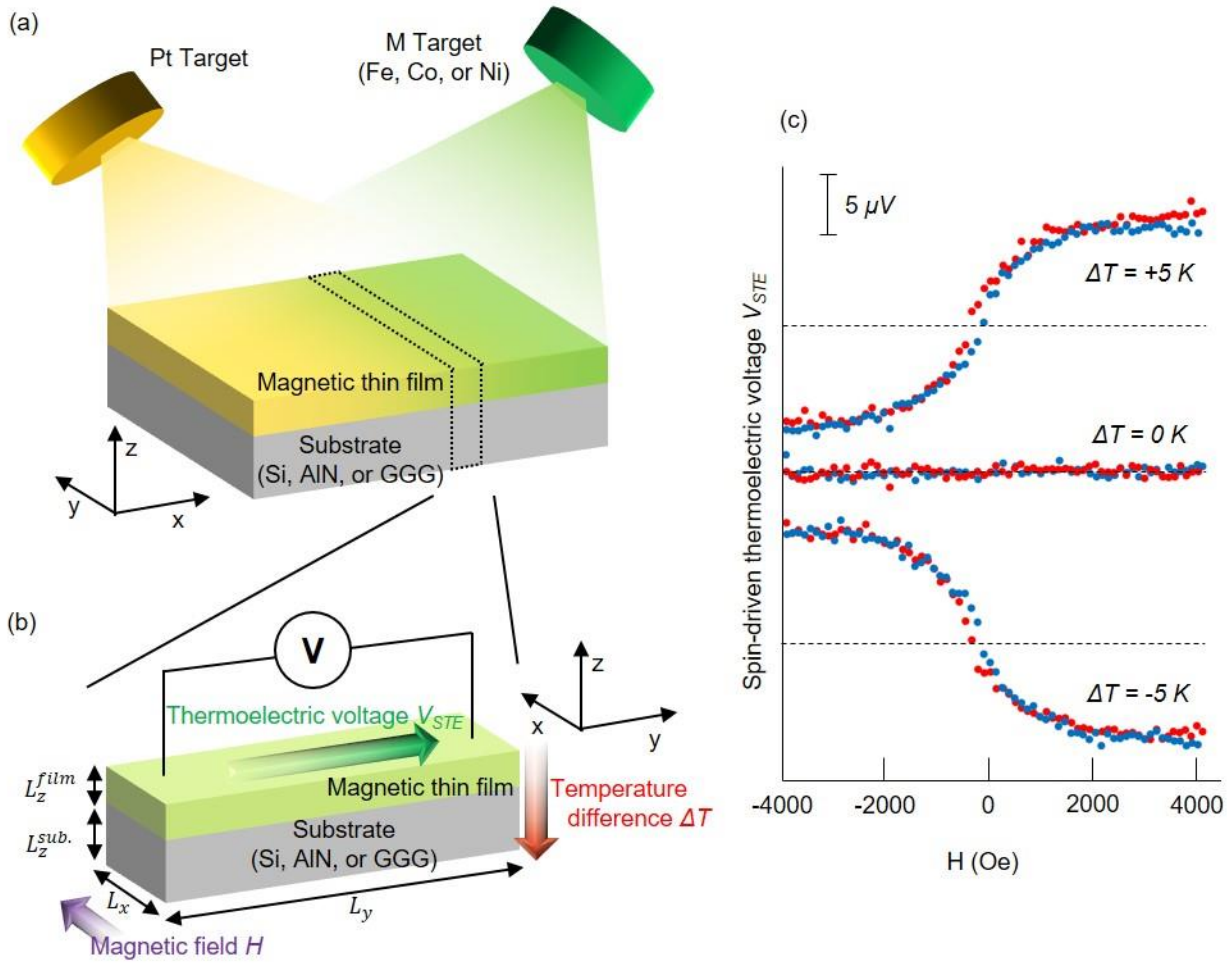

Supplementary Figure 1 | Experimental data of thermopower S_{STE}. Data of spin-driven thermopower S_{STE} was obtained by combinatorial experiments. **a.** Schematic of combinatorial sputtering method. **b.** Schematic of spin-driven thermoelectric (STE) device using anomalous Nernst effect (ANE). c. STE voltage V_{STE} of STE device ($Ni_{88.3}Pt_{11.7}$/GGG sample) as function of H.

In addition to these experimental data, we also have carried out a conventional material simulation, density function theory (DFT) calculation, to obtain a lot of material parameters (descriptors) ***X*.** A Korringa-Kohn-Rostoker coherent potential approximation (KKR-CPA) method using AkaiKKR software [5] was used for the DFT

calculation. With the composition information obtained from the combinatorial XRF experiment, the DFT calculations were carried out for all possible crystal structures. For instance, fcc, bcc, and $L1_0$ structures are the possible crystal structures in FePt binary alloy, which were determined by the combinatorial XRD experiments.

Before analyzing these data with machine learning, we should note that the materials of experimental data S_{STE} are strictly different from those of the DFT calculation data even if their compositions are the same due to their crystal structural differences. The materials fabricated in the combinatorial sputtering are polycrystalline. On the other hand, the DFT calculations were performed assuming single crystal structures. Therefore, data-preprocessing was performed to decrease the crystal structural differences between the experimental data S_{STE} and the DFT calculation data. Supplementary Figure 2 shows the data-preprocessing for the case of the Fe orbital angular moment in the FePt binary alloy system. Firstly, based on the composition information obtained from the combinatorial XRF experiments, the Fe orbital angular moments were simulated by the DFT calculations for each composition and possible crystal structures (fcc, bcc, and $L1_0$), as shown in Supplementary Figure 2 (a). Secondly, the combinatorial XRD experiments were performed to obtain crystal structure information. Supplementary Figure 2 (b) shows the x-ray diffraction (XRD) curves including crystal structure information for each composition. Thirdly, one of the non-supervised machine learnings, non-negative matrix factorization (NMF), was applied to these XRD curves. It is known that the NMF decomposes the XRD curves into single crystal XRD curves. Accordingly, it quantifies the crystal structural rates [6]. Supplementary Figure 2 (c) shows the crystal structural rates of the FePt binary alloy system. Fe-rich materials include large amounts of bcc structure while Pt-rich materials have large amounts of fcc structure. The $L1_0$-ordered structure appears around Fe:Pt = 1:1 composition. These results are consistent with our intuitive understanding from the viewpoint of

material science. Finally, the Fe orbital angular moments calculated by the DFT calculations were compensated by the crystal structure rates. In this case, we calculated the weighted sum of the Fe orbital moment with the structural rates as the weights. The compensated results are shown with the purple lines in Supplementary Figure 2 (a). This data-preprocessing was performed on all of the calculation data so that we could obtain the materials parameter sets $\mathbf{X} \equiv \{X_1, X_2, X_3 \ldots X_{14}\}$.

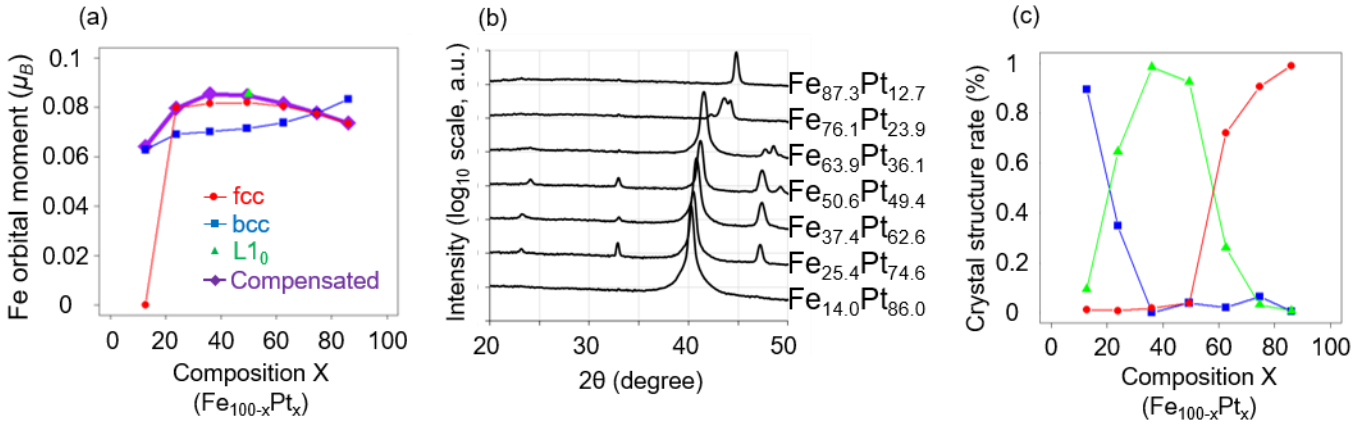

Supplementary Figure 2 | Data-preprocessing. a. Fe orbital moment calculated ab-initio (KKR-CPA method) in $Fe_{100-x}Pt_x$ binary alloy with respect to each possible crystal structure (fcc: red, bcc: blue, and $L1_0$: green). Data compensated by data-preprocessing are plotted as purple. **b.** XRD curves of $Fe_{100-x}Pt_x$ binary alloy obtained by combinatorial XRD measurement. **c.** Crystal structure rates in $Fe_{100-x}Pt_x$ binary alloy estimated by non-negative matrix factorization (NMF).

X_1 and X_2 denote the atomic percentage (at%) of the magnetic atom M (M = Fe, Co, or Ni) and Pt atom in the materials, respectively. X_3 and X_4 mean the spin moment and orbital moment of the M atom, while X_5 and X_6 are those of the Pt atom. X_7 and X_8 show the M and Pt spin polarization calculated by one of the DFT results, a projected density of state (DoS). X_3, X_4, X_5, X_6, X_7, and X_8 descriptors are expected to give us some spin-related

information in the machine learning modelling. On the other hand, X_9, X_{10}, X_{11}, and X_{12} are thermo-related descriptors as follows. X_9 and X_{10} denote the DoS slope of the M and Pt atom on the Fermi level E_F. X_{11} is the difference between the up-spin DoS slope and the down-spin DoS slope of the M atom on the E_F, while X_{12} shows that of the Pt atom. The X_9, X_{10}, X_{11}, and X_{12} descriptors are expected to give us some thermo-related descriptions in the machine learning modelling because thermoelectric phenomena are related to the DoS behavior in the vicinity of the Fermi level E_F [7]. X_{13} and X_{14} are selected based on the current fundamental knowledge of the spin-driven thermoelectric phenomena, the anomalous Nernst effect (ANE). X_{13} is a spin-orbit interaction (coupling) energy, which is known as an origin of the ANE [8]. X_{14}, the average spin moment ($X_1X_3 + X_2X_4$), was purposely created since it is proportional to the magnetization. Accordingly, it is proportional to the ANE thermopower S_{STE} [9,10].

Supplementary Discussion

Because of the high interpretability of the FAB/HMEs, we can interpret the data-driven model based on our material science knowledge. It would be interesting to note the inconsistency between the data-driven model and current material science because it may possibly reflect an unknown side of material science and accordingly give us some inputs and impetus for new scientific discoveries.

As described in the main text, we notice that the material data is firstly classified according to the average spin moment (X_{14}) at gate 1, as shown in Figure 4(a). The material data with a small average spin moment X_{14} go to the component 1, where the thermopower S_{STE} is equal to zero (S_{STE} = 0, as shown in Figure 4b). On the other hand, the material data with a large X_{14} go to gate 2 followed by gate 3, component 2, component 3, and

component 4, in which the S_{STE} are finite values. This classification can be readily explained by the ANE basic mechanism. The ANE basically appears on magnetic materials. The materials with small magnetization (i.e. a small average spin moment X_{14}) do not have the ANE with the exception of a few antiferromagnetic materials [9]. Therefore, this data-classification is really trivial knowledge and is consistent with the material science of the ANE.

Secondly, the magnetic materials data is classified by experimental conduction term **C**, the kind of substrates, at gate 2 and gate 3 in the FAB/HMEs data-driven model. The magnetic materials data on the Si, AlN, and GGG substrates belong to component 2, component 3, and component 4, respectively. This classification can also be understood by a simple mechanism. In our experimental setup, the temperature gradient is applied between the top of the magnetic films and the bottom of the substrates. Therefore, the temperature gradient applied in the substrates is parasitic thermal resistance, whose temperature gradient does not contribute to the thermopower S_{STE}. Substrates with higher thermal conductivity have larger S_{STE}. This classification is also consistent with our intuitive understanding.

Thirdly, we notice that there is a positive correlation between the thermopower S_{STE} and the product term X_2X_8, where X_2 and X_8 are the Pt concentration and Pt spin polarization, respectively. This correlation, which was disclosed by the machine learning for the first time, appears to be beyond our current knowledge of ANE. Although it is known that the S_{STE} is almost proportional to the saturation magnetization M_s in the whole material (average spin moment X_{14}) [9,10], it is non-trivial that the amount of the specific local spin polarization contributes to the ANE. This correlation implies that the local spin polarization of a large spin-orbit interaction element, such as Pt, can enhance the ANE. This interpretation seems not to be so far from the intuition of scientists in the spin

caloritronics field. However, the explanation for this correlation has not yet been reported clearly based on theoretical physics.

Fourthly, we found a negative correlation between the thermopower S_{STE} and the product term X_6X_{13}, where X_6 and X_{13} are the orbital moment of Pt atom and spin-orbit interaction energy, respectively. Note that the value of spin-orbit interaction energy X_{13} is negative, therefore this correlation means that the S_{STE} increases with increasing of spin-orbit interaction energy (i.e. decreasing of X_{13} value). It is natural that the larger spin-orbit interaction energy results in larger S_{STE} because the spin-orbit interaction is the origin of ANE. On the other hand, the correlation between the X_6 and S_{STE} is a non-trivial knowledge for ANE. Although we developed the STE materials by using the positive X_2X_8 term as an indicator in the main text, it would be possible to further improve the S_{STE} by considering the negative X_6X_{13} term in the future.

The interpretable machine learning, FAB/HMEs, disclosed the surprising positive correlation between S_{STE} and X_2X_8. Therefore, searching materials with large X_2X_8 can lead to the discovery of ANE materials with improved S_{STE}. It is quite difficult to perform the material screening for large S_{STE} by ab-initio calculation because the fundamental mechanism of the ANE has not been completely established yet. On the other hand, the material screening for large X_2X_8 is feasible since we can easily simulate the X_2X_8 by ab-initio (KKR-CPA) calculation.

We expected that the X_2X_8 would be enhanced by expanding lattice constant of CoPt alloy, in which we have observed the largest thermopower S_{STE} so far. In order to confirm that, we investigated a CoPtN system whose lattice constant is expected to be larger than that of CoPt because N atom is inserted into the center of CoPt fcc structure [11].

One of the DFT calculations, the KKR-CPA method, was used to simulate the X_2X_8 of the CoPtN system. The calculation was performed on a perovskite structure [11], where N atoms and Co-Pt disordered atoms are located in a body-centered position and other positions (face-centered and vertex position), respectively. The N concentration at the body-centered position was represented as a mixture of N atoms and vacant atoms by coherent potential approximation (CPA), which was also used to represent the Co-Pt disordered atom. Supplementary Figure 3 shows the Pt spin polarization X_8 in $Co_{50}Pt_{50}N_x$ as a function of N concentration x. The Pt spin polarization increases with increasing N concentration. Therefore, we can expect that the $Co_{50}Pt_{50}N_{10}$ with large Pt spin polarization X_8 has a large thermopower S_{STE}.

For experimental confirmation, we have actually fabricated some $Co_{50}Pt_{50}N_x$ thin films with different N concentration by the sputtering process. The co-sputtering with a Co and Pt target was performed in Ar+N atmosphere with different N partial pressure at room temperature. Figure 5 shows the experimental S_{STE} results of these $Co_{50}Pt_{50}N_x$ films. It is clear that the S_{STE} increases with increasing X_2X_8 accompanying N concentration. The compositions were determined by X-ray photoelectron spectroscopy (XPS). Although we have also tried to increase the N concentration more by increasing the N partial pressure, the N concentration in the actual $Co_{50}Pt_{50}N_x$ thin films has not achieved this at 10 % in our experiments. Nevertheless, the S_{STE} of $Co_{48.9}Pt_{51.1}N_{7.2}$ is at 13.04 μV/K, which is larger than that of the current generation of STE materials [9,10]. By increasing the N concentration with other fabrication methods, further enhancement of the S_{STE} may be possible in the CoPtN system in the future.

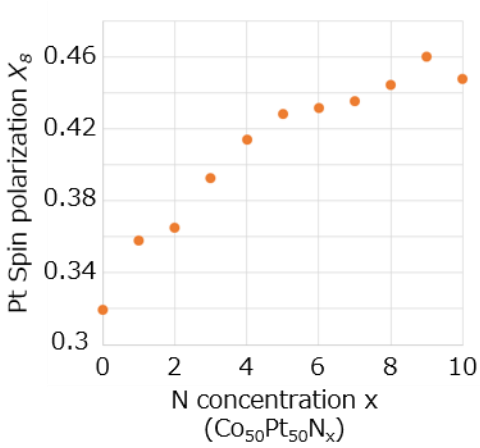

Supplementary Figure 3 | Materials screening guided by FAB/HMEs informed knowledge. Pt spin polarization X_8 in $Co_{50}Pt_{50}N_x$ as function of N concentration x calculated by ab-initio (KKR-CPA method) calculation.

Supplementary Reference

1. Koinuma, H. & Takeuchi, I. Combinatorial solid-state chemistry of inorganic materials. Nat. Mater. **3,** 429 (2004)

2. Takeuchi, I. et al. Identification of novel compositions of ferromagnetic shape-memory alloys using composition spreads. Nat. Mater. **2,** 180-184 (2003)

3. Sakuraba, Y. Potential of thermoelectric power generation using anomalous Nernst effect in magnetic materials. Scr. Mater. **111,** 29 (2016)

4. Uchida, K. et al. Thermoelectric Generation Based on Spin Seebeck Effects. Proc. IEEE **104,** 1946 (2016)

5. Akai, H. Electronic Structure Ni-Pd Alloys Calculated by the Self-Consistent KKR-CPA Method. J. Phys. Soc. Jpn. **51,** 468-474 (1982)

6. Kusne, A. G. et al. On-the-fly machine-learning for high-throughput experiments: search for rare-earth-free

permanent magnets. Sci. Rep. **4,** 6367 (4014)

7. Goldsmid, H. J. *Introduction to Thermoelectricity* (Springer, 2010).

8. Hasegawa, K. et al. Material dependence of anomalous Nernst effect in perpendicularly magnetized ordered-alloy thin films. Appl. Phys. Lett. **106,** 252405 (2015)

9. Ikhlas, M. et al. Large anomalous Nernst effect at room temperature in a chiral antiferromagnet. Nat. Phys. **13,** 1085-1090 (2017)

10. Guin, S. N. et al. Anomalous Nernst ettect beyond the magnetization scaling relation in the ferromagnetic Heusler compound Co_2MnGa. NPJ Asia Mater. **11,** 16 (2019)

11. Meinert, M. et al. Exchange interactions and Curie temperatures of the tetrametal nitrides Cr_4N, Mn_4N, Fe_4N, Co_4N and Ni_4N. J. Phys: Condens. Matter **28,** 056006 (2016)